Journal of Materials Research and Technology 39 (2025) 7036–7050

Contents lists available at ScienceDirect

Journal of Materials Research and Technology

journal homepage: www.elsevier.com/locate/jmrt

Dual-scale modeling of temperature-dependent deformation and damage in martensitic steels

Zhen Zhang [a], Sebastian Münstermann [a], Fuhui Shen [a,b,*]

[a] Institute of Metal Forming, RWTH Aachen University, Intzestraße 10, D-52072, Aachen, Germany
[b] Ghent University, Department of Electromechanical, Systems and Metal Engineering, Soete Laboratory, Technologiepark 46, 9052, Zwijnaarde, Belgium

ARTICLE INFO

Keywords:
Martensitic steel
Dual-scale modeling
Localization
Temperature
Stress triaxiality
Lattice reorientation

ABSTRACT

Understanding the deformation and failure of martensitic steels under extreme service conditions is critical for ensuring the safety and reliability of industrial tooling and structural components. In this study, tensile tests were conducted on a low-carbon martensitic steel at 297 K, 193 K, and 133 K using specimens designed to induce different levels of stress triaxiality. A dual-scale modeling framework, integrating continuum mechanics with crystal plasticity (CP) simulations, was developed to investigate temperature-dependent deformation localization and failure. Macroscopic fracture properties of the material are captured using a damage mechanics approach, whilst the underlying microscopic deformation behavior was analyzed using CP modeling with a hierarchical representative volume element (RVE). Results reveal that improved local ductility at lower temperatures is stress state-dependent, with minimal temperature influence on texture evolution. Shear-dominated loading (low stress triaxiality) induces significant lattice reorientation, enhancing near rot-goss $\{110\}\langle 332\rangle$ and near brass $\{331\}\langle 136\rangle$ components, whereas uniaxial and notch tension (moderate/high triaxiality) lead to limited, uniform rotations. Grains with initial γ-fiber orientations are prone to strain localization under shear loading. These findings provide a clearer understanding of the multiscale deformation and failure behavior of martensitic steels under complex loading and offer guidance for the design and application of these materials in engineering environments.

1. Introduction

Low-carbon (< 0.6 wt. %) martensitic steels featuring lath martensite structures are widely used tool materials for industrial applications owing to their exceptional strength and wear resistance [1–3]. Lath martensite with a body-centered cubic (bcc) structure containing high dislocation density forms through diffusionless displacive transformation of face-centered cubic (fcc) austenite on habit planes, generating a hierarchical microstructure composed of prior austenite grain (PAG), packet, block and lath with particular topological and orientation relationships [4,5]. While lath martensite is deemed to be hard and brittle, martensitic steels can deform in a ductile manner with large macroscopic plastic deformation under uniaxial tension even at cryogenic temperatures [2,6–8]. A comprehensive understanding of deformation and damage behavior necessitates the characterization of material responses covering different stress states from shear to notch tension. Distinct stress states can be reached by introducing unique specimen geometries, as commonly practiced in damage mechanics investigations [9–14]. However, the fracture properties of martensitic steels with such complex structures have not been fully exploited for distinct stress states and temperatures in the literature, representing a critical knowledge gap in the field.

Currently, experimental techniques have limitations in quantitative analysis of deformation behaviors at finer scales, such as texture evolution. Crystal plasticity (CP) models, explicitly accounting for the deformation kinematics of individual crystals, are capable of capturing the lattice rotation of crystal matrices and the resultant evolving texture in combination with the representative volume element (RVE) [15]. Texture evolution is potentially influenced by the initial crystallographic orientation, stress state and temperature [16–21]. For instance, CP simulations have been employed to study tensile deformation in 9Cr–1Mo martensitic steel with different initial textures [17] and to interpret temperature impacts on the texture transformation in AA6082 aluminum alloy [18]. Studies on materials, such as α-Ti, have further

* Corresponding author. Ghent University, Department of Electromechanical, Systems and Metal Engineering, Soete Laboratory, Technologiepark 46, 9052, Zwijnaarde, Belgium.

E-mail addresses: fuhui.shen@ibf.rwth-aachen.de, fuhui.shen@ugent.be (F. Shen).

https://doi.org/10.1016/j.jmrt.2025.11.015
Received 1 April 2025; Received in revised form 30 October 2025; Accepted 3 November 2025
Available online 4 November 2025

Table 1
Chemical composition of the martensitic steel, wt. %.

C	Mn	Si	Cr	Al	Ni	Ti	Nb	P	Fe
0.173	1.420	0.407	0.347	0.041	0.029	0.027	0.013	0.012	Bal.

stressed that the sensitivity of texture evolution to temperature can vary significantly depending on the dominant deformation mechanism (e.g., twinning vs slip) [19]. Additionally, a through process CP-static recrystallization model has proven effective in capturing recrystallized textures in AA6063 aluminum alloy under compression loading [22]. These studies demonstrate the reliability and convenience of CP methods for investigating interior texture evolution that is challenging to access experimentally. Nonetheless, the majority of microscopic deformation investigations are limited to ambient and elevated temperatures under a particular ideal stress state. This neglects the influence of different stress states on the texture evolution at cryogenic temperatures, thereby leaving a gap in understanding the coupled effects of stress state and cryogenic temperature on texture evolution, despite being highly relevant for engineering applications. In addition, incorporating real complex loading conditions is imperative for accurate deformation and failure analysis.

Coarse-scale models are inadequate for capturing microstructural variation, whereas fine-scale models face limitations in reflecting realistic macroscopic constraints and computational costs, rendering it difficult to fully uncover deformation localization related to failure at a single length scale. In the context of multi-scale and multi-physics integrated computational materials engineering (ICME), two approaches are leveraged to establish structure-property linkages, i.e., bottom-up [23,24] and top-down [25–28] strategies. The former deduces homogenized mechanical properties from knowledge of the local microstructure, with a high demand for computational resources. Fang et al. [24] introduced a hierarchical multi-scale framework relying on molecular dynamics, discrete dislocation dynamics and crystal plasticity finite element (CPFE) simulations to capture the macroscopic hardening behavior of materials from nano-micro-mesoscale physical mechanisms. Conversely, the top-down approach starts from a coarse scale and relocalizes stress and strain fields to evaluate heterogeneities within the material, which is well-suited for analyzing various kinds of macroscale boundary value problems with finite elements (FEs) [29]. This approach has been utilized in studies ranging from predicting fatigue life of notched components [30] to investigating shear band formation [31] and post-necking deformation [27,32]. These applications emphasize that the top-down approach is highly effective in tracing the origin of macroscopic behaviors across scales. Nevertheless, the top-down approach has not yet been systematically applied to decouple stress state effects on local deformation responses at cryogenic temperatures. Therefore, developing a cross-scale scheme capable of continuously tracking deformation localization up to failure is essential for understanding the behavior of martensitic steels under complex loadings at cryogenic temperatures.

To fill the aforementioned gaps, in this work, we develop a top-down macro-microscale modeling framework integrating macroscopic damage mechanics with phenomenological CP modeling via displacement mapping. The fracture properties of a low-carbon martensitic steel are characterized across temperatures using optimized specimen geometries. With a hierarchical RVE, macroscopic stress state effects on lattice reorientation are systematically explored down to the level of individual grains. The remainder of the paper is organized as follows. Section 2 describes the martensitic steel, PAG reconstruction and macroscopic mechanical tests. Section 3 introduces the top-down macro-microscale methodology and theoretical basis. Section 4 elaborates on the

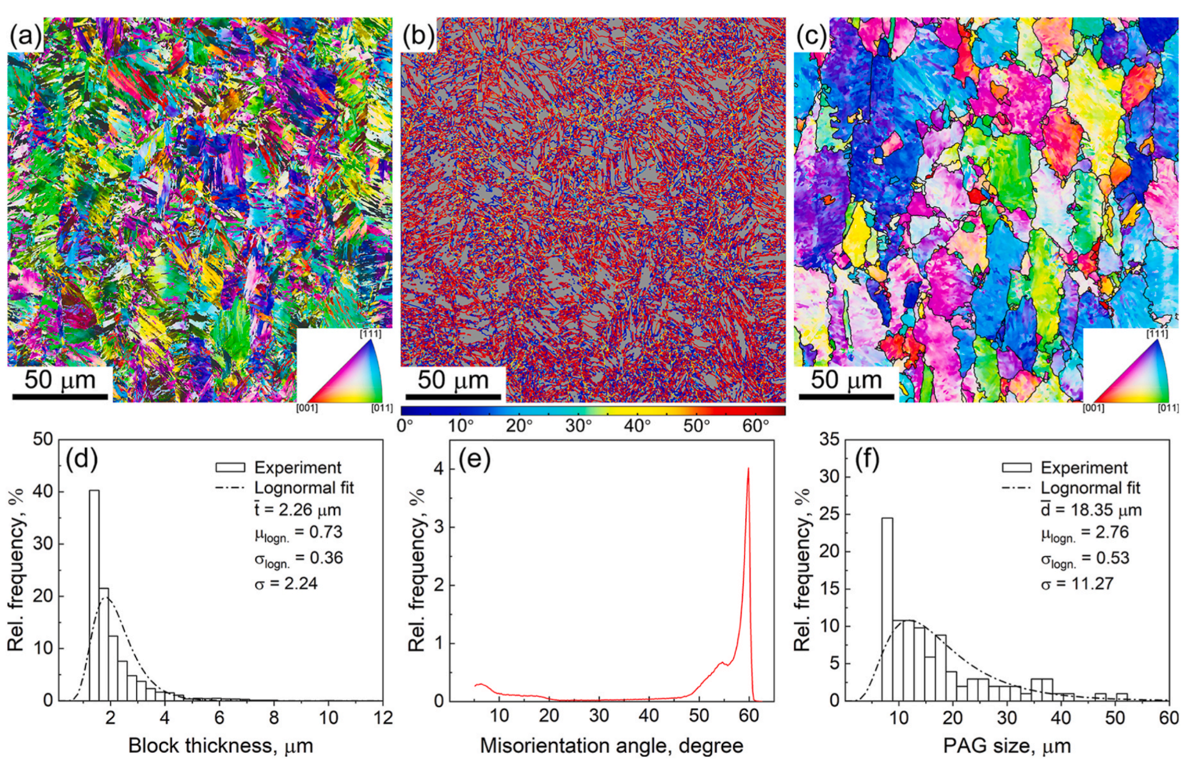

Fig. 1. Microstructure reconstruction scheme: (a) crystallographic orientation map of the investigated material along RD (step size: 150 nm); (b) misorientation angle distribution of the EBSD scanned area in (a); (c) IPF-X map of the reconstructed PAG based on the refined OR ($\{31\bar{2}\}_{\gamma}//\{12\bar{1}\}_{\alpha'}$ and $\langle 112\rangle_{\gamma}//\langle 012\rangle_{\alpha'}$); (d)–(f) corresponding statistics for (a)–(c). The fitting parameters of the grain size lognormal distributions are also summarized in (d) and (f).

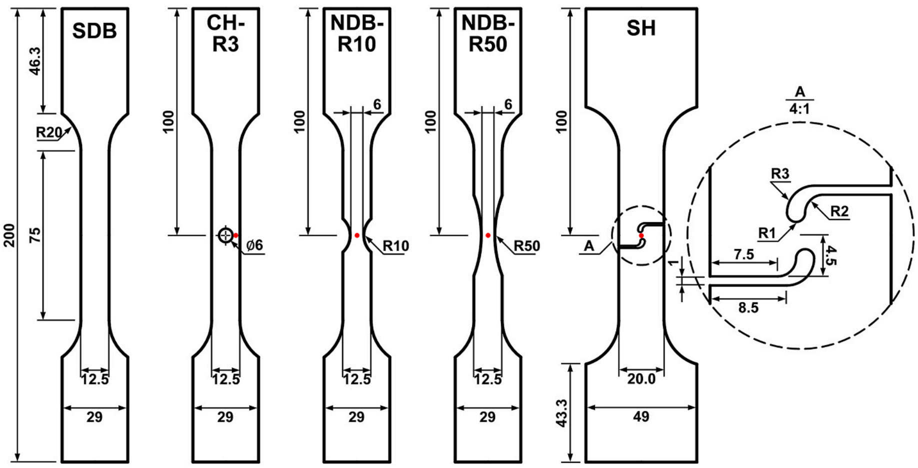

Fig. 2. Dimensions of all specimen geometries for mechanical characterization at room and cryogenic temperatures (unit in mm). Critical regions (CRs) of fracture in CH, NDB and SH specimens are highlighted by red dots.

temperature dependence of deformation localization and failure in the material at different stress triaxialities. Section 5 ends the paper with some concluding remarks.

2. Material and mechanical tests

A hot-rolled low-carbon martensitic steel plate, austenitized at 1223 K for 15 min, followed by water quenching to room temperature and then tempered at 473 K for 60 min, was utilized in the current work. The chemical composition determined by wet chemical analysis is listed in Table 1. To achieve lath martensite structure, a relatively low C content (~0.173 wt. %) is adopted, while the addition of a high Mn content (~1.420 wt. %) promotes the strength and wear resistance of the steel. The initial microstructure was characterized on the rolling direction-transverse direction (RD-TD) plane of 0.05 μm active oxide polishing suspension (OP–S) polished square specimen ($15 \times 15 \times 2$ mm^3) using electron backscatter diffraction (EBSD, Oxford Instruments Nordlys-Nano) with a step length of 150 nm at an accelerating voltage of 20 kV in a scanning electron microscope (SEM, Carl Zeiss GeminiSEM). The EBSD data collected in an area of 200×200 μm^2 were analyzed with MATLAB crystallographic toolbox MTEX v5.8 add-on ORTools [33]. Fig. 1 (a) reveals the typical fine substructure of the martensitic steel in the inverse pole figure (IPF) map parallel to RD (IPF-X), and the misorientation angle distribution is showcased in Fig. 1 (b). A block boundary misorientation threshold of 5° was set, and with a hybrid variant graph algorithm [34], clusters of blocks that belong to the same PAG were identified. Following the fine-tuned Kurdjumov-Sachs relation [21,35], i.e., $\{31\overline{2}\}_\gamma//\{12\overline{1}\}_{\alpha'}$ and $\langle 112\rangle_\gamma//\langle 012\rangle_{\alpha'}$, the crystallographic orientations of PAGs are iteratively back-calculated from the EBSD data and depicted in Fig. 1 (c). Statistical analysis of block thickness, misorientation angle and PAG size are accordingly given in Fig. 1 (d)–(f), where the lognormal probability density function ($f\left(x\middle|\mu_{\mathrm{logn.}},\sigma_{\mathrm{logn.}}\right) = \frac{1}{x\sigma_{\mathrm{logn.}}\sqrt{2\pi}}\exp\left[-\frac{\left(\ln x-\mu_{\mathrm{logn.}}\right)^2}{2\sigma^2_{\mathrm{logn.}}}\right]$, $\mu_{\mathrm{logn.}}$ and $\sigma_{\mathrm{logn.}}$ are the mean and standard deviation of logarithmic values, respectively) was used to quantify the grain size distribution, and the standard deviation of values is assessed by $\sigma = \sqrt{\exp\left(2\mu_{\mathrm{logn.}}+\sigma^2_{\mathrm{logn.}}\right)\left[\exp\left(\sigma^2_{\mathrm{logn.}}\right)-1\right]}$. In total, 2165 blocks and 102 PAGs were collected with the mean grain size of 2.26 μm and 18.35 μm, respectively. Further information on the prior austenite reconstruction is provided by Ref. [21].

To capture the stress state and temperature dependence of fracture properties, 2 mm thick flat specimens with varying geometries were sectioned from the position at 1/3 of the thickness of the 8 mm steel plate by wire-electrode cutting. Fig. 2 displays all specimen geometries for tensile tests, including smooth dog-bone (SDB) specimen, central

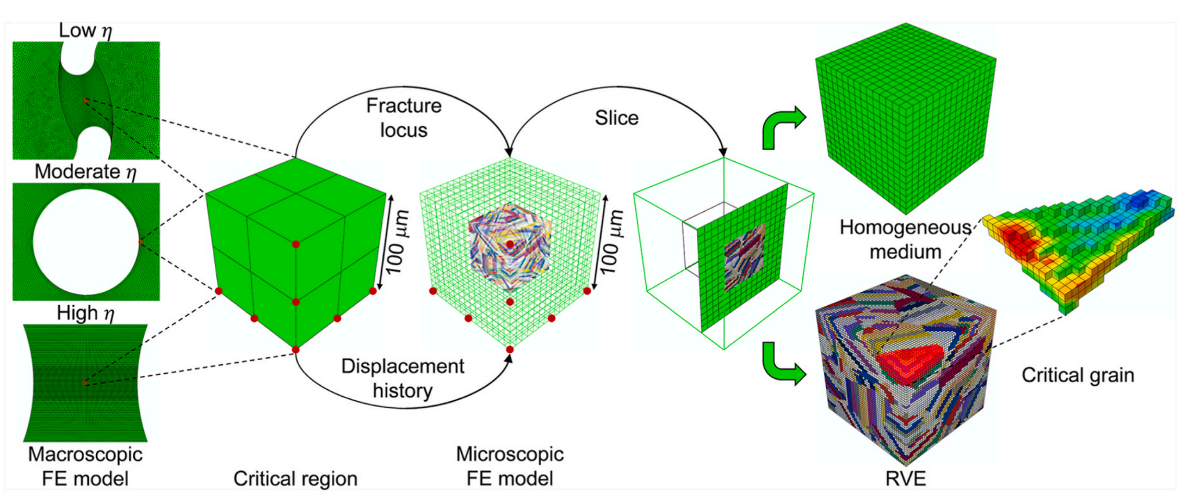

Fig. 3. Schematic of the sequential dual-scale modeling in CRs of fracture in SH (low η), CH (moderate η) and NDB (high η) geometries. Please note that the slice is provided solely for enhanced visualization of the microscopic FE model.

hole (CH) specimen with a 3 mm radius circular cutout in the center (CH-R3), notched dog-bone (NDB) specimens with notch radii of 10 mm (NDB-R10) and 50 mm (NDB-R50) and shear (SH) specimen. Note that CH-R3 specimen features a stress state close to uniaxial tension while ensuring localization. Tensile tests were conducted on all specimens with a gauge length of 50 mm at various temperatures (297 K, 193 K and 133 K) by a universal tensile machine (Zwick/Roell Z250) in accordance with DIN EN ISO 6892-1/3 standards [36,37]. The targeted cryogenic conditions were reached with liquid nitrogen cooling, and all specimens were immersed in the temperature environments for 15 min prior to testing. A thermocouple was attached to the specimen to monitor the surface temperature. Constant crosshead velocities of 0.45 mm/min for SDB specimens and 0.2 mm/min for notched specimens were imposed to achieve comparable quasi-static loadings. The temperature curves were recorded during testing (see Appendix A). For each scenario, at least two repeats were executed, and all tests were carried out along RD since the macroscopic anisotropy in the material is not pronounced by evaluating the r-value (an indicator of anisotropy) being ~0.85 (close to 1) at necking strain [21].

3. Dual-scale methodology and theoretical basis

3.1. Methodology

The proposed macro-microscale modeling approach for investigating deformation localization and failure follows a top-down strategy, as illustrated in Fig. 3. At the macroscale, the FE model was discretized using C3D8R elements with a fine element size of 50 μm in the critical region (CR, 100 × 100 × 100 μm^3). The accuracy of macroscopic FE models with varying stress states is assessed by comparing force-displacement responses with experimental results. To simulate local deformation behaviors with more realistic boundary conditions (BCs), displacement histories are extracted from the CR and passed to corresponding nodes in the same-sized microscopic FE model (100 × 100 × 100 μm^3) as input BCs. The critical strain based fracture locus determined from macroscale simulations is used as a global fracture indicator at the microscale. In the context of CPFE simulations, periodic boundary conditions (PBCs) are frequently implemented in RVEs with periodicity to avoid over-constraints on edges and vertices [38]. However, the regions of interest (i.e., CRs) in this study correspond to finite regions rather than infinite plates, where the strain distributions are non-periodic, rendering the use of PBCs inappropriate. In this regard, the microscopic FE model, consisting of a central RVE and a surrounding homogeneous medium, mitigates numerical over-constraints at the surface for adaptive and smooth transfer of BCs. The homogeneous medium was discretized using C3D8R elements with an element size of 6.67 μm. The RVE of size 48 × 48 × 48 μm^3 was constructed and discretized into 110592C3D8R elements using DRAGen software [39]. Tie-surface constraints are applied to connect the homogeneous medium with the RVE. The intrinsic material responses accounting for varying stress triaxiality histories can thus be probed down to the grain level. An uncoupled damage mechanics model is used in macroscopic FE simulations. In microscale simulations, the homogeneous medium is described using the identical yield function and hardening law as that used for macroscale simulations, and a phenomenological CP model incorporating the Hall-Petch relation is applied to simulate the deformation of the RVE. Dual-scale simulations were performed using ABAQUS software.

3.2. Macroscale model

The macroscopic mechanical degradation of the martensitic steel is described by the hybrid damage mechanics model, i.e., modified Bai-Wierzbicki (MBW) model, proposed by Lian et al. [11]. The stress triaxiality (η) and Lode angle parameter ($\overline{\theta}$), two dimensionless parameters, are widely utilized to characterize the stress state, which are derived from the first invariant (I_1) of the Cauchy stress tensor ($\boldsymbol{\sigma}$) and the second (J_2) and third (J_3) invariants of the corresponding deviatoric stress tensor ($\boldsymbol{s}$),

$$I_1 = \mathrm{tr}\boldsymbol{\sigma},\ J_2 = \frac{1}{2}\boldsymbol{s}:\boldsymbol{s},\ J_3 = \det(\boldsymbol{s}),\ \boldsymbol{s} = \boldsymbol{\sigma} - (\mathrm{tr}\boldsymbol{\sigma}/3)\mathbf{I} \tag{1}$$

$$\eta = \frac{\sigma_{\mathrm{m}}}{\overline{\sigma}},\ \overline{\theta} = 1 - \frac{2}{\pi}\arccos\left(\frac{3\sqrt{3}}{2}\frac{J_3}{J_2^{3/2}}\right) \tag{2}$$

with the hydrostatic stress ($\sigma_{\mathrm{m}} = \frac{I_1}{3}$) and von Mises equivalent stress ($\overline{\sigma} = \sqrt{3J_2}$).

Assuming the material is elastic-plastic with isotropic hardening and plastic incompressibility, the yield function can be formulated as

$$f = \overline{\sigma}(\boldsymbol{\sigma}) - (1-D)\sigma_{\mathrm{y}}(\overline{\varepsilon}^{\mathrm{p}}, \overline{\theta}) \le 0 \tag{3}$$

$$\sigma_{\mathrm{y}}(\overline{\varepsilon}^{\mathrm{p}}, \overline{\theta}) = \sigma_{\mathrm{y}}(\overline{\varepsilon}^{\mathrm{p}})\left[c_\theta^{\mathrm{s}} + \left(c_\theta^{\mathrm{ax}} - c_\theta^{\mathrm{s}}\right)\left(\gamma - \frac{\gamma^{c_\theta^{\mathrm{m}}+1}}{c_\theta^{\mathrm{m}}+1}\right)\right] \tag{4}$$

$$\gamma = \frac{\sqrt{3}}{2-\sqrt{3}}\left[\sec\left(\frac{\overline{\theta}\pi}{6}\right) - 1\right] \tag{5}$$

$$c_\theta^{\mathrm{ax}} = \begin{cases} c_\theta^{\mathrm{t}}, & \overline{\theta} \ge 0 \\ c_\theta^{\mathrm{c}}, & \overline{\theta} < 0 \end{cases} \tag{6}$$

where D is a scalar variable between zero and one to indicate the damage status of the material, i.e., zero for the undamaged state and one for the complete fracture state. $\sigma_{\mathrm{y}}(\overline{\varepsilon}^{\mathrm{p}})$ denotes the reference flow curve. c_θ^{s}, c_θ^{t}, c_θ^{c} and c_θ^{m} are material constants to describe the effect of the Lode angle parameter on plasticity. Specifically, c_θ^{s}, c_θ^{t}, c_θ^{c} are the normalized strength under shear, tension and compression states, and c_θ^{m}, a non-negative integer, is the smoothness index of the yield surface. Neglecting the strength differential effect in the material by taking $c_\theta^{\mathrm{s}} = c_\theta^{\mathrm{t}} = c_\theta^{\mathrm{c}} = 1$, the yield function is reduced to

$$f = \overline{\sigma}(\boldsymbol{\sigma}) - (1-D)\sigma_{\mathrm{y}}(\overline{\varepsilon}^{\mathrm{p}}) \le 0 \tag{7}$$

The plastic deformation is described by von Mises yield function before damage initiation ($D = 0$), in conjunction with a conventional associated flow rule,

$$\dot{\varepsilon}^{\mathrm{p}} = \dot{\lambda}\frac{\partial f}{\partial \sigma} \tag{8}$$

where $\dot{\lambda}$ is the non-negative plastic multiplier to update strain components. A linear combination of Swift and Voce isotropic hardening laws is applied to describe the flow behavior for a broad strain range, given as

$$\sigma_{\mathrm{y}}(\overline{\varepsilon}^{\mathrm{p}}) = w\sigma_{\mathrm{Swift}}(\overline{\varepsilon}^{\mathrm{p}}) + (1-w)\sigma_{\mathrm{Voce}}(\overline{\varepsilon}^{\mathrm{p}}) \tag{9}$$

$$\sigma_{\mathrm{Swift}}(\overline{\varepsilon}^{\mathrm{p}}) = A(\overline{\varepsilon}^{\mathrm{p}} + \varepsilon_0)^{\mathrm{n}},\ \sigma_{\mathrm{Voce}}(\overline{\varepsilon}^{\mathrm{p}}) = k_0 + Q\left(1 - e^{-\beta\overline{\varepsilon}^{\mathrm{p}}}\right) \tag{10}$$

with hardening parameters (A, ε_0, n, k_0, Q and β) and weighting factor (w) requiring calibration.

The overall stress state can be represented by the strain-averaged η and $\overline{\theta}$,

$$\eta_{\mathrm{avg}} = \frac{1}{\overline{\varepsilon}^{\mathrm{p}}}\int_0^{\overline{\varepsilon}^{\mathrm{p}}} \eta(\overline{\varepsilon}^{\mathrm{p}})d\overline{\varepsilon}^{\mathrm{p}},\ \overline{\theta}_{\mathrm{avg}} = \frac{1}{\overline{\varepsilon}^{\mathrm{p}}}\int_0^{\overline{\varepsilon}^{\mathrm{p}}} \overline{\theta}(\overline{\varepsilon}^{\mathrm{p}})d\overline{\varepsilon}^{\mathrm{p}} \tag{11}$$

A cut-off value of $-1/3$ for η (i.e., $\eta_{\mathrm{c}} = -\frac{1}{3}$) is integrated into the damage mechanics model, below which damage and fracture shall be completely suppressed owing to high hydrostatic pressure [40]. The strain-based damage initiation and fracture criteria ($\overline{\varepsilon}_{\mathrm{d}}^{\mathrm{p}}$ and $\overline{\varepsilon}_{\mathrm{f}}^{\mathrm{p}}$) are expressed as

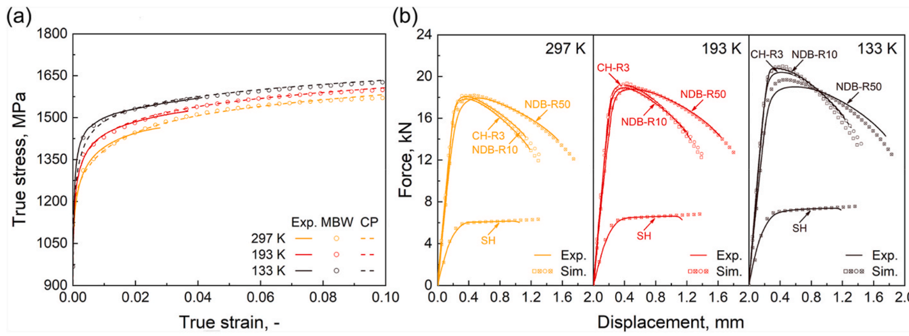

Fig. 4. (a) Calibration of flow behaviors in MBW and CP models based on uniaxial tensile properties at temperatures of 297 K, 193 K and 133 K; (b) prediction of force-displacement curves of tensile tests using von Mises plasticity criterion with the calibrated Swift-Voce hardening at various temperatures.

$$\bar{\varepsilon}_{\mathrm{d}}^{\mathrm{p}}(\eta,\bar{\theta}) = \begin{cases} +\infty, & \eta \le \eta_{\mathrm{c}} \\ \left(D_1 e^{-D_2\eta} - D_3 e^{-D_4\eta}\right)\bar{\theta}^2 + D_3 e^{-D_4\eta}, & \eta > \eta_{\mathrm{c}} \end{cases} \tag{12}$$

$$\bar{\varepsilon}_{\mathrm{f}}^{\mathrm{p}}(\eta,\bar{\theta}) = \begin{cases} +\infty, & \eta \le \eta_{\mathrm{c}} \\ \left(F_1 e^{-F_2\eta} - F_3 e^{-F_4\eta}\right)\bar{\theta}^2 + F_3 e^{-F_4\eta}, & \eta > \eta_{\mathrm{c}} \end{cases} \tag{13}$$

with four damage parameters (D_1, D_2, D_3 and D_4) and four fracture parameters (F_1, F_2, F_3 and F_4) requiring calibration. In practice, proportional loading states are challenging to realize. To compensate to some extent for the non-proportional loading effects, the damage and fracture indicators (I_{d} and I_{f}) are introduced to quantify the accumulation degree of damage and fracture [41],

$$I_{\mathrm{d}} = \int_0^{\bar{\varepsilon}^{\mathrm{p}}} \frac{d\bar{\varepsilon}^{\mathrm{p}}}{\bar{\varepsilon}_{\mathrm{d}}^{\mathrm{p}}(\eta,\ \bar{\theta})} \tag{14}$$

$$I_{\mathrm{f}} = \int_{\bar{\varepsilon}_{\mathrm{d}}^{\mathrm{p,c}}}^{\bar{\varepsilon}^{\mathrm{p}}} \frac{d\bar{\varepsilon}^{\mathrm{p}}}{\bar{\varepsilon}_{\mathrm{f}}^{\mathrm{p}}(\eta,\ \bar{\theta}) - \bar{\varepsilon}_{\mathrm{d}}^{\mathrm{p}}(\eta,\ \bar{\theta})} \tag{15}$$

Damage is triggered when $I_{\mathrm{d}} = 1$, and then the damage accumulates until the final fracture occurs when $I_{\mathrm{f}} = 1$. The damage variable (D) is consequently described as

$$D = \begin{cases} 0, & I_{\mathrm{d}} < 1 \\ \dfrac{\bar{\sigma}_{\mathrm{d}}^{\mathrm{c}}}{G_{\mathrm{f}}}\left(\bar{\varepsilon}_{\mathrm{f}}^{\mathrm{p}} - \bar{\varepsilon}_{\mathrm{d}}^{\mathrm{p}}\right) I_{\mathrm{f}}, & I_{\mathrm{d}} \ge 1 \wedge I_{\mathrm{f}} < 1 \\ 1, & I_{\mathrm{d}} \ge 1 \wedge I_{\mathrm{f}} \ge 1 \end{cases} \tag{16}$$

where $\bar{\sigma}_{\mathrm{d}}^{\mathrm{c}}$ is equivalent plastic stress at damage initiation strain ($\bar{\varepsilon}_{\mathrm{d}}^{\mathrm{p,c}}$), and G_{f} is the material parameter that controls damage evolution, taken as 100 MPa for all macroscale simulations for simplicity.

3.3. Microscale model

A phenomenological CP model based on dislocation slip, as detailed in Ref. [15], is adopted. The kinematic description of finite strain elastoplasticity follows a multiplicative decomposition of the deformation gradient ($\mathbf{F}$) into an elastic stretch and lattice rotation part ($\mathbf{F}_{\mathrm{e}}$) and a plastic part ($\mathbf{F}_{\mathrm{p}}$),

$$\mathbf{F} = \mathbf{F}_{\mathrm{e}}\ \mathbf{F}_{\mathrm{p}} \tag{17}$$

$$\dot{\mathbf{F}}_{\mathrm{p}} = \mathbf{L}_{\mathrm{p}}\ \mathbf{F}_{\mathrm{p}} \tag{18}$$

where $\mathbf{L}_{\mathrm{p}}$ is the plastic velocity gradient relevant to the dislocation motion on slip system α. It can be calculated from the sum of the shear strain rate ($\dot{\gamma}^{\alpha}$) over the total number of active slip systems (N),

$$\mathbf{L}_{\mathrm{p}} = \sum_{\alpha=1}^{\mathrm{N}} \dot{\gamma}^{\alpha}\mathbf{s}^{\alpha} = \sum_{\alpha=1}^{\mathrm{N}} \dot{\gamma}^{\alpha}(\mathbf{m}^{\alpha} \otimes \mathbf{n}^{\alpha}) \tag{19}$$

where $\mathbf{s}^{\alpha} = \mathbf{m}^{\alpha} \otimes \mathbf{n}^{\alpha}$ is the Schmid tensor for the slip direction vector $\mathbf{m}^{\alpha}$ and slip plane normal vector $\mathbf{n}^{\alpha}$ on slip system α, and $\otimes$ represents the dyadic product. The following rate-dependent power-law flow rule is employed to relate $\dot{\gamma}^{\alpha}$ to the resolved shear stress (τ^{α}) and the critical resolved shear stress (CRSS, $\tau_{\mathrm{c}}^{\alpha}$) on slip system α,

$$\dot{\gamma}^{\alpha} = \dot{\gamma}_0 \left|\frac{\tau^{\alpha}}{\tau_{\mathrm{c}}^{\alpha}}\right|^{\nu} \mathrm{sgn}(\tau^{\alpha}) \tag{20}$$

where $\dot{\gamma}_0$ is the reference shear strain rate, taken as 0.001 s^{-1}, and parameter ν stands for the strain rate sensitivity (SRS) exponent of slip. τ^{α} on slip system α is defined as

$$\tau^{\alpha} = \mathbf{S} : (\mathbf{m}^{\alpha} \otimes \mathbf{n}^{\alpha}) \tag{21}$$

where $\mathbf{S}$ is the second Piola-Kirchhoff tensor and can be deduced from $\mathbf{F}_{\mathrm{e}}$,

$$\mathbf{S} = \frac{1}{2}\mathbb{C} : \left(\mathbf{F}_{\mathrm{e}}^{\mathrm{T}}\mathbf{F}_{\mathrm{e}} - \mathbf{I}\right) \tag{22}$$

where $\mathbb{C}$ accounts for the fourth-order anisotropic elasticity tensor, and $\mathbf{I}$ indicates the second-order identify tensor. For cubic crystals, $\mathbb{C}$ is specified in terms of three elastic constants (C_{11}, C_{12} and C_{44}). The influence of slip system β on the hardening behavior of slip system α is given as

$$\dot{\tau}_{\mathrm{c}}^{\alpha} = \sum_{\beta=1}^{\mathrm{N}} h_{\alpha\beta}\left|\dot{\gamma}^{\beta}\right| \tag{23}$$

with the hardening matrix ($h_{\alpha\beta}$) evolving as

$$h_{\alpha\beta} = q_{\alpha\beta}\left[h_0\left(1 - \frac{\tau_{\mathrm{c}}^{\beta}}{\tau_{\mathrm{c}}^{\mathrm{s}}}\right)^{a}\right] \tag{24}$$

where $q_{\alpha\beta}$ is the ratio of the latent hardening rate ($\alpha \ne \beta$) to the self-hardening rate ($\alpha = \beta$); h_0, $\tau_{\mathrm{c}}^{\mathrm{s}}$ and a correspond to the initial hardening rate, saturation CRSS and hardening exponent, which are assumed to be identical for considered 24 slip systems ($12 \times \{110\}\langle 111\rangle$ and $12 \times \{112\}\langle 111\rangle$) at room and cryogenic temperatures in bcc steels. Other slip systems ($24 \times \{123\}\langle 111\rangle$) in bcc steels are difficult to activate and can be neglected for computational efficiency [42,43]. $q_{\alpha\beta}$ value is generally taken as 1.0 for coplanar slip systems and 1.4 for non-coplanar slip systems. The hardening evolution law of slip system α is formulated as

$$\tau_{\mathrm{c}}^{\alpha} = \tau_0 + \int_0^{\mathrm{t}} q_{\alpha\beta}\left[h_0\left(1 - \frac{\tau_{\mathrm{c}}^{\beta}}{\tau_{\mathrm{c}}^{\mathrm{s}}}\right)^{a}\right]\left|\dot{\gamma}^{\beta}\right| dt \tag{25}$$

The initial CRSS (τ_0) as a function of grain size can be described by the Hall-Petch relation [44],

Table 2
Calibration of flow curve parameters at 297 K, 193 K and 133 K.

Temperature	A	ε_0	n	k_0	Q	β	w
297 K	1720	1.0e^{-6}	0.074	1367	267.7	45.8	0.336
193 K	1795	1.0e^{-6}	0.067	1439	205.0	38.5	0.400
133 K	1815	1.0e^{-6}	0.086	1377	386.0	898.0	0.500

$$\tau_0 = \hat{\tau}_0 + \frac{K}{\sqrt{d}} \tag{26}$$

where $\hat{\tau}_0$ is the size-independent initial CRSS, K is the strengthening modulus, and d is the grain diameter.

4. Sequential modeling and investigations

4.1. Macroscale modeling

A crucial prerequisite for leveraging the macroscale model lies in determining plasticity and fracture parameters to accurately reflect the temperature-dependent mechanical behaviors of the investigated material. To this end, one-half FE models of four tensile geometries (SH, CH-R3, NDB-R10 and NDB-R50) were constructed considering through-thickness symmetry, and displacement-controlled loading was applied. The von Mises plasticity criterion with Swift-Voce hardening, i.e., MBW model omitting the strength differential effect on plasticity, was leveraged to describe macroscopic plastic deformation. The calibrated flow curves based on uniaxial tensile properties before necking at temperatures of 297 K, 193 K and 133 K are shown in Fig. 4 (a), and the associated parameters are given in Table 2. As the temperature decreases, the yield strength increases due to the enhanced resistance to dislocation motion (e.g., Peierls stress) at lower temperatures, which elevates the stress required for initial yielding [6]. The strain hardening slightly diminishes with declining temperature since the temperature dependence of dislocation multiplication and annihilation leads to the variation in dislocation density, as qualitatively presented in Fig. 5. With the extrapolated flow curves, the simulated force-displacement results of the tensile tests with four representative geometries at three different temperatures are compared with experimental results in Fig. 4 (b). The predicted results confirm that the calibrated macroscopic flow behavior provides reasonable accuracy in capturing the plasticity of the martensitic steel until fracture. Only distinct differences can be found at 133 K, especially for CH-R3 and NDB-R50 cases with maximum deviations of 0.62 kN (3.06 %) and 0.91 kN (6.44 %) at displacements of 0.42 mm and 1.75 mm.

The direct experimental measurement of local stress fields in critical regions of these specimens is extremely challenging. Although local strain fields can be obtained from digital image correlation, this technique is limited to surface observations, while the critical fracture point is located within the specimen interior. Consequently, the evolution of local stress and strain variables until fracture is extracted from critical elements in SH, CH and NDB geometries via finite element analysis. As a sudden drop of the applied force is considered to be the damage initiation and fracture point in this study, the uncoupled damage mechanics approach is adopted, where the damage initiation and fracture criteria are assumed to be identical (i.e., $\bar{\varepsilon}_d^p = \bar{\varepsilon}_f^p$). The local stress state variables (η_{avg} and $\bar{\theta}_{avg}$) and equivalent plastic strain (PEEQ) at fracture at 297 K, 193 K and 133 K are accordingly collected in Table 3. The fracture parameters that are equal to damage parameters in the uncoupled MBW model are calibrated in Table 4, and the variation of strain-based fracture locus with temperature is illustrated in Fig. 6 (a), where the local stress state evolution in four different geometries is also shown. It is observed that a decline in temperature enhances local ductility non-monotonically because of a rise in fracture strain, and the local ductility enhancement is stress state dependent. A pronounced Lode angle parameter dependence of the fracture strain can also be concluded at all temperatures. To validate macroscopic fracture parameters, the predicted fracture behavior of the martensitic steel across temperatures using the uncoupled damage mechanics approach is compared with their experimental results in Fig. 6 (b). The fracture displacements are accurately predicted by the calibrated fracture criteria with a maximum deviation in fracture displacement being only 0.085 mm (4.86 %) in the case of NDB-R50 at 133 K. This implies a good predictive capability of the macroscopic mechanics model for fracture behavior within the considered temperature and stress state ranges.

4.2. CP modeling

To configure an adequate set of microscopic material parameters of the martensitic steel, the constructed hierarchical RVE contains 37 PAGs

Table 3
Local stress and strain variables at fracture across temperatures.

Temperature	Geometry	η_{avg}	$\bar{\theta}_{avg}$	PEEQ
297 K	SH	0.047	−0.006	0.772±0.014
	CH-R3	0.377	0.906	1.102±0.028
	NDB-R10	0.713	0.343	0.698±0.011
	NDB-R50	0.653	0.530	0.764±0.011
193 K	SH	0.052	−0.005	0.790±0.006
	CH-R3	0.380	0.898	1.197±0.025
	NDB-R10	0.729	0.330	0.727±0.012
	NDB-R50	0.666	0.513	0.804±0.010
133 K	SH	0.063	−0.004	0.907±0.004
	CH-R3	0.389	0.868	1.263±0.008
	NDB-R10	0.724	0.353	0.846±0.004
	NDB-R50	0.748	0.419	0.905±0.011

Table 4
Calibration of fracture parameters in MBW model across temperatures.

Temperature	F_1	F_2	F_3	F_4
297 K	1.537	0.317	0.813	0.289
193 K	1.578	0.295	0.867	0.268
133 K	1.678	0.213	0.946	0.202

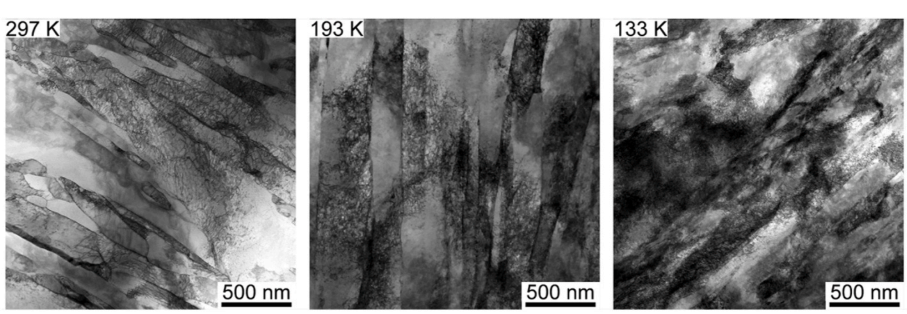

Fig. 5. Transmission electron microscope (TEM) bright field images of the tensile deformed SDB specimens at 297 K, 193 K and 133 K qualitatively showing dislocation density increases with decreasing temperature [2].

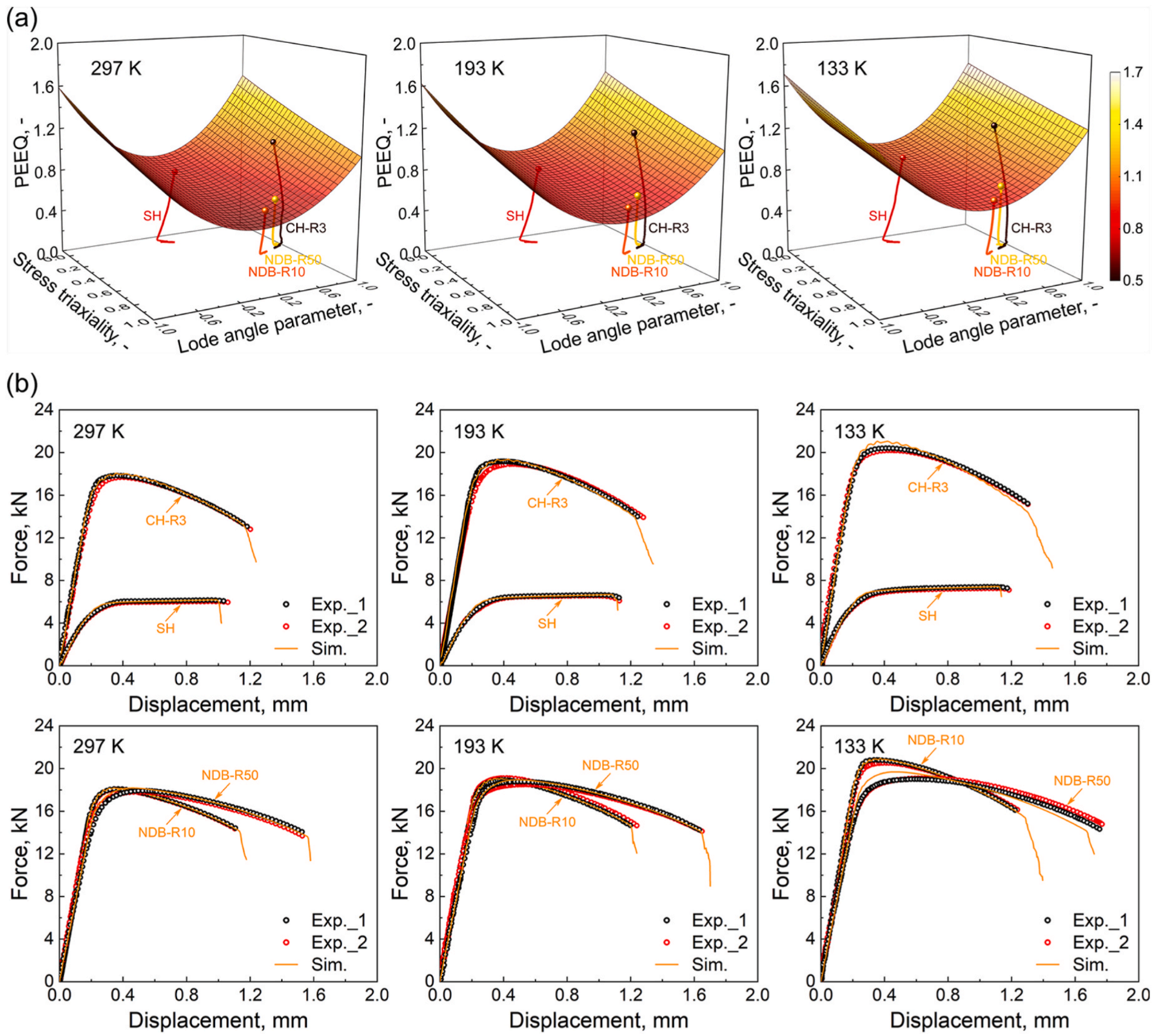

Fig. 6. (a) Fracture loci of the martensitic steel at 297 K, 193 K and 133 K; (b) prediction of temperature-dependent fracture behaviors in tensile tests with various geometries using the calibrated MBW model.

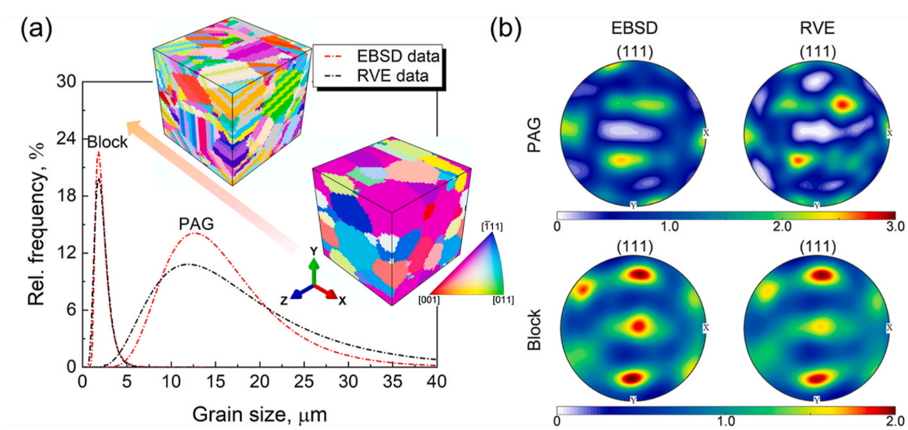

Fig. 7. Comparison of EBSD and RVE data collected at PAG and block levels for (a) grain size lognormal distributions and (b) crystallographic orientation distributions in the form of (111) PF. Insets in (a) are the same RVE colored according to IPF-X at PAG and block levels, respectively.

and 809 corresponding blocks and is colored according to IPF-X at each level, as displayed in Fig. 7. The statistics of microstructural features with respect to grain size and crystallographic orientation basically coincides with the measured results obtained from the EBSD scanned area in Fig. 1. However, it is observed in Fig. 7 (a) that the deviation in grain size lognormal distribution at the PAG level is slightly large, which is a result of the computational precision-efficiency trade-off. Specifically, an extremely high mesh resolution of blocks and a sufficiently large number of PAGs required are incompatible in the current numerical simulations. A mesh sensitivity analysis can be found in Appendix B.

Table 5
CP parameters for the martensitic steel at room temperature (297 K) [21].

Elastic constants			SRS	Slip hardening			Hall-Petch relation	
C_{11}	C_{12}	C_{44}	ν	h_0	τ_c^s	a	$\widehat{\tau}_0$	K
297.4 GPa	127.5 GPa	85.0 GPa	116.3 –	1667 MPa	1247 MPa	8.0 –	321 MPa	300 MPa· $\sqrt{\mu m}$

Within CP model, the associated parameters at 297 K identified in Ref. [21] are summarized in Table 5. A weak temperature dependence of the elastic constants (C_{11}, C_{12} and C_{44}) is ignored for simplicity. The rest temperature-dependent parameters (h_0, τ_c^s and $\widehat{\tau}_0$) are dictated by inverse optimization of global flow behaviors before necking at temperatures of 297 K, 193 K and 133 K based on the volume-averaged homogenization method [21]. From Fig. 4 (a), the simulated flow curves align well with their experimental counterparts as well as predicted results by the macroscopic mechanics model. Three adjustable parameters related to temperature are given in Fig. 8 and interpolated with double logarithmic functions for their estimation in the temperature range of 133 K–297 K, expressed as

$$h_0(T) = 5795.0 \ln(0.2356 \ln T) \tag{27}$$

$$\tau_c^s(T) = -635.9 \ln(0.0248 \ln T) \tag{28}$$

$$\widehat{\tau}_0(T) = -124.3 \ln(0.0134 \ln T) \tag{29}$$

where T is temperature in Kelvin. It is explicit that both τ_c^s and $\widehat{\tau}_0$ decrease with increasing temperature, while h_0 exhibits an opposite trend and a more pronounced susceptibility to temperature changes.

4.3. Consistency analysis

In cross-scale modeling in Fig. 3, ensuring the consistency between macroscale and microscale models after calibration is essential for accurately probing intrinsic material responses. The principal strain histories (maximum, medium and minimum), evaluated from CRs of NDB-R10 (high η), CH-R3 (moderate η) and SH (low η) upon different temperatures (297 K, 193 K and 133 K), are compared with those averaged over the corresponding RVEs. It is evident from Fig. 9 that excellent agreement in average principal strain history is achieved. Moreover, the evolving history of average η over RVEs in Fig. 10 is indicative of reasonable matching with macroscopic counterparts in all cases, verifying the consistency between the calibrated CP and macroscopic constitutive behaviors. It should be noted that marginal discrepancies in η histories between the two scales are inevitable since displacement history serves as a bridge correlating macroscale and microscale simulations. Besides, owing to the practical impossibility of experimentally measuring local mechanical responses inside specimens, CP parameters in this study are calibrated solely from uniaxial tensile results, which might result in stress deviations to varying extents in other stress states [45,46]. In Fig. 10, the MBW predicted fracture loci under plane stress conditions ($\sigma_2 = 0$ or $\sigma_3 = 0$) [47] are plotted in red

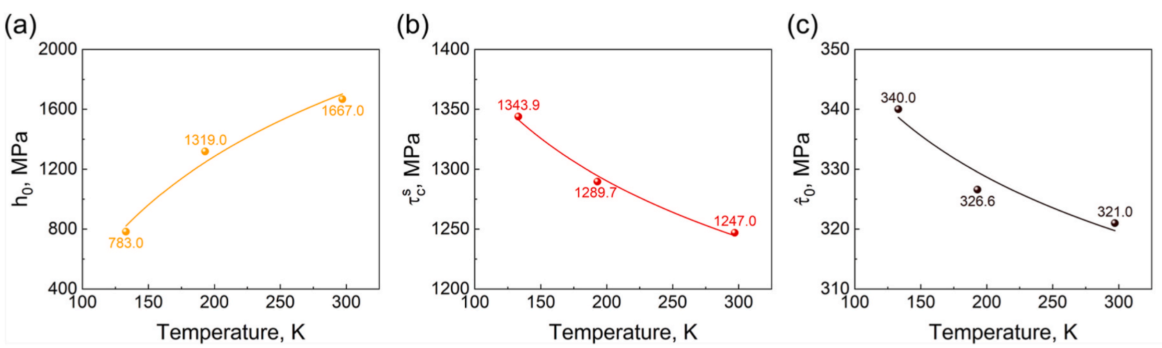

Fig. 8. Temperature-dependent CP parameter distributions of (a) initial hardening rate, (b) saturation CRSS and (c) size-independent initial CRSS. Calibrated values at 297 K, 193 K and 133 K are also noted beside dots.

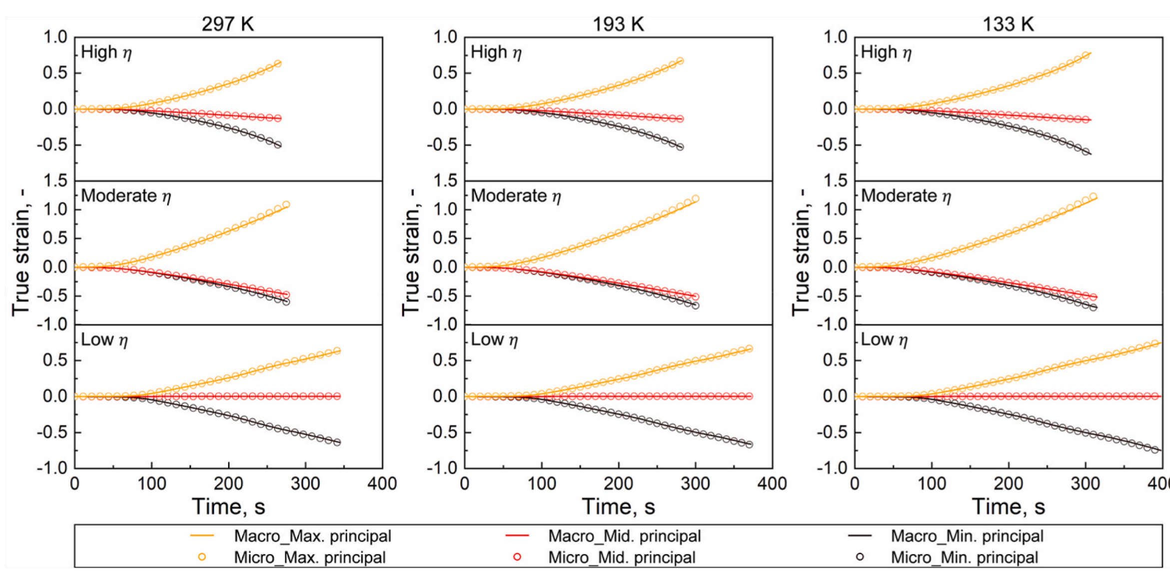

Fig. 9. Comparison of average principal strain histories in CRs of macroscopic FE models with high, moderate and low η and their corresponding RVEs at 297 K, 193 K and 133 K.

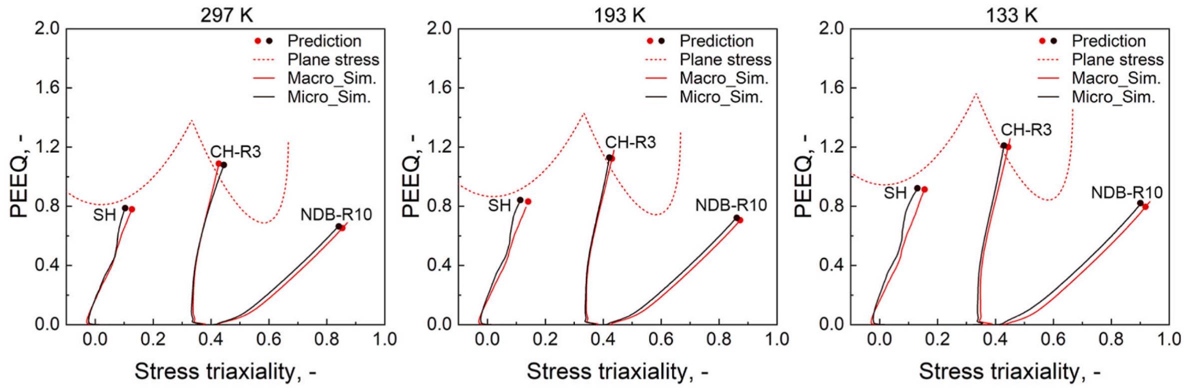

Fig. 10. Comparison of average η histories in CRs of macroscopic FE models and their corresponding RVEs at 297 K, 193 K and 133 K. Red dashed lines denote MBW predicted fracture loci for plane stress conditions. Red and black dots signify MBW predicted fracture points according to full loading paths (red and block lines).

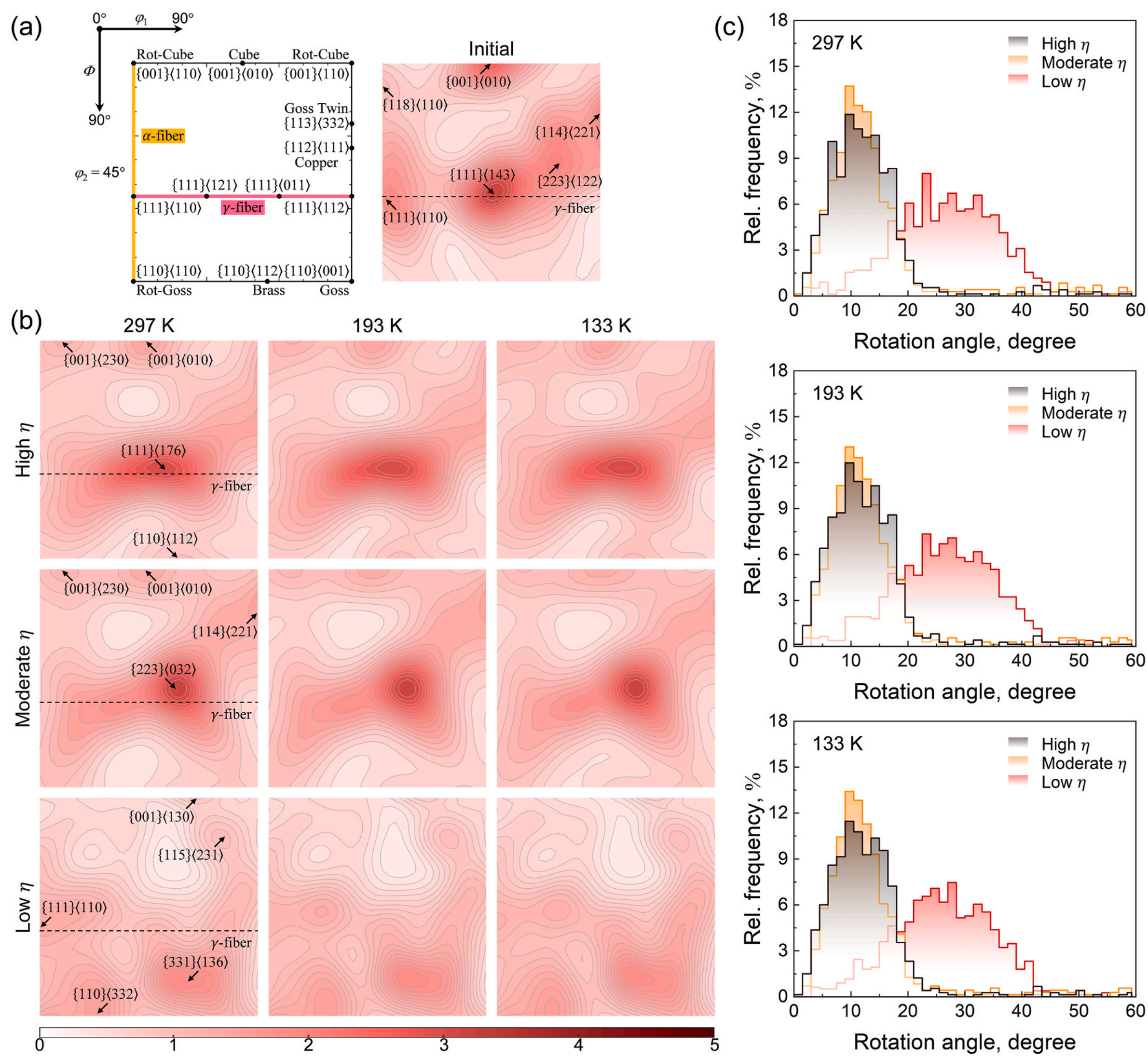

Fig. 11. (a) ODF sections at $\varphi_2 = 45^\circ$ showing main ideal orientations in bcc steels (left) and orientation distributions in initial RVE (right); (b) ODF sections at $\varphi_2 = 45^\circ$ showing orientation distributions in deformed RVEs ($\varepsilon^{g}_{vM} = 0.6$) subjected to high, moderate and low η histories at 297 K, 193 K and 133 K; (c) associated rotation angle showing angular deviation from initial state. The same color scale bar is used in (a) and (b).

dashed lines for three different temperatures. SH and CH-R3 geometries exhibit small changes in stress triaxiality during deformation, while NDB-R10 geometry experiences continuous change of stress states until fracture, showcasing a significantly non-proportional loading history. The fracture points for global RVE responses (black dots) are also predicted by the identified fracture loci in Fig. 6, which are very close to the predicted fracture points for local macroscopic responses (red dots) with acceptable deviations.

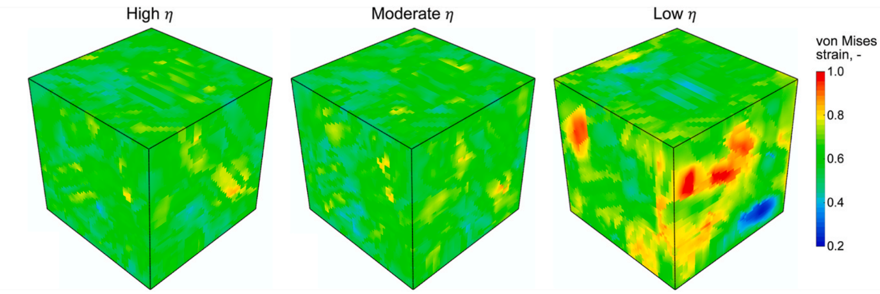

Fig. 12. Comparison of strain heterogeneities in deformed RVEs at ε^{g}_{vM} of 0.6 under different stress states.

4.4. Lattice reorientation in polycrystals

Plastic deformation via slip on activated slip systems is accompanied by the lattice rotation of crystal matrices toward preferred orientations [32,48], which may exhibit differing stress state and temperature dependence. The ideal texture components in bcc steels and orientation distribution in the constructed RVE are illustrated in Fig. 11 (a) in the form of $\varphi_2 = 45^\circ$ sections of the orientation distribution function (ODF). Relatively strong textures of γ-fiber (i.e., $\{111\}\langle143\rangle$, $\{111\}\langle110\rangle$ and $\{223\}\langle122\rangle$) and cube $\{001\}\langle010\rangle$ are detected in the initial RVE, along with weak textures of near rotated cube (rot-cube) $\{118\}\langle110\rangle$ and near goss twin $\{114\}\langle221\rangle$. Fig. 11 (b) depicts ODF sections at $\varphi_2 = 45^\circ$ for deformed RVEs (0.6 global von Mises strain, $\varepsilon^{g}_{vM} = 0.6$) subjected to high, moderate and low η loadings at 297 K, 193 K and 133 K. For each η, no substantial changes in orientation with temperature is observed due to similar slip modes. This coincides with the research reported in Refs. [49–51] and indicates that strain heterogeneity ought to be similar at all considered temperatures. For each temperature, it is evident that texture evolution is dependent on the stress state. Nonetheless, the main texture components are less evolving at high and moderate η. Both cases possess relatively strong textures of γ-fiber (i.e., $\{111\}\langle176\rangle$ for high η and $\{223\}\langle032\rangle$ for moderate η) and cube $\{001\}\langle010\rangle$ with a slight decrease in intensity, wherein the orientation spread along γ-fiber is more significant at high η. Ibragimova et al. [52] also stressed that texture evolution is not significant under uniaxial tension (i.e., moderate η in this study). At low η, noticeable orientation spreads lead to altered main texture components compared with the undeformed state, and there is a decrease in overall intensity, even though the intensity in near rotated goss (rot-goss) $\{110\}\langle332\rangle$ and near brass $\{331\}\langle136\rangle$ textures increase. Apparently, shear deformation manifests more complexity in comparison with high and moderate η loadings.

On the other hand, to reach the same ε^{g}_{vM}, the distribution of the associated rotation angle relative to the initial orientation in Fig. 11 (c) suggests that high and moderate η cases are disinclined to maintain the coordination of plastic deformation through lattice rotation, resulting in subtle orientation changes. In contrast, the larger and more non-uniformly distributed rotation angle at each temperature demonstrates inferior deformation resistance of the material under intense shear loading, thus weakening initial texture and promoting heterogeneous deformation, as shown in Fig. 12. Taylor factor, as an indicator to estimate the resistance to deformation, can be computed with respect to the local deformation gradient and crystallographic orientation of individual grains using MTEX v5.8 [53,54]. Note that different stress states induce significantly distinct deformation gradients, and local deformation gradients among grains may vary even under the same overall stress state [55]. As summarized in Table 6, the calculated average Taylor factor over virtual polycrystalline aggregate at low η is always the lowest and almost constant, regardless of temperature and strain, which corroborates to some extent the distribution of rotation angle since a large number of grains possessing relatively low Taylor factors are indeed favorably oriented for activating slip systems and the resultant apparent lattice rotation to accommodate severe plastic deformation [56].

Table 6
Average Taylor factors for the martensitic steel before and after deformation under various configurations.

Stress state	297 K		193 K		133 K	
	$\varepsilon^{g}_{vM} = 0$	$\varepsilon^{g}_{vM} = 0.6$	$\varepsilon^{g}_{vM} = 0$	$\varepsilon^{g}_{vM} = 0.6$	$\varepsilon^{g}_{vM} = 0$	$\varepsilon^{g}_{vM} = 0.6$
High η	2.90	2.87	2.89	2.88	2.86	2.89
Moderate η	2.92	2.94	2.93	2.94	2.92	2.92
Low η	2.60	2.61	2.61	2.63	2.62	2.61

4.5. Lattice reorientation in critical grain

As failure is associated with strain localization [8,57], the critical grain (CG) characterized by the high-strained region at fracture is extracted from the RVE under each configuration. Note that the location of CG and its lattice reorientation behavior do not differ with temperature but with stress state from the current simulation results, and hence only temperature of 297 K is considered in this subsection. In Fig. 13 (a), ODF sections at $\varphi_2 = 45^\circ$ depict orientation variation with deformation for three CGs (CG1, CG2 and CG3, identified under high, moderate and low η loadings, respectively) with initial orientations of (140.7°, 116.6°, 217.4°), (321.9°, 97.0°, 329.7°) and (52.8°, 52.6°, 32.3°). It can be seen that, as deformation proceeds, the orientation inside CG1 is slightly displaced from near γ-fiber $\{223\}\langle334\rangle$ toward $\{112\}\langle132\rangle$ with a decrease in overall intensity. CG2 rotates away from near α-fiber $\{113\}\langle691\rangle$ to $\{112\}\langle372\rangle$ component with an increase in overall intensity. CG3 rotates approaching γ-fiber with a rise in intensity, then spreads away from it and concentrates in $\{441\}\langle234\rangle$ component. The orientation that evolves in the CG seems quite unstable under low η loading in comparison with the former two cases, which is also reflected by the lattice rotation trajectory of CGs in (111) PFs in Fig. 13 (b). The evolving Taylor factor with strain in CGs are calculated in Fig. 14, demonstrating that the high-strained region is biased in favor of the grain featuring a relatively low Taylor factor under each stress state. The average Taylor factors during deformation are 2.85, 2.79 and 2.37 for CG1, CG2 and CG3, respectively, implying the highest chance of activating slip systems and the lowest stress to resist deformation for the CG identified under global shear loading. Such discrepancy arises from the synergistic effect of different initial orientations and local kinematics (e.g., grain interaction) [58]. It is notable that the current observations of lattice reorientation rely heavily on numerical predictions. More experimental validations are needed once the associated technical challenges are addressed.

4.6. Strain and stress states in critical grain

To track the changes in strain and stress states from a microscopic perspective up to the failure moment, the dependence of average local strain over CG on the global strain of RVE and the associated η evolution are assessed. For each grain, marginal discrepancies in local strain and η

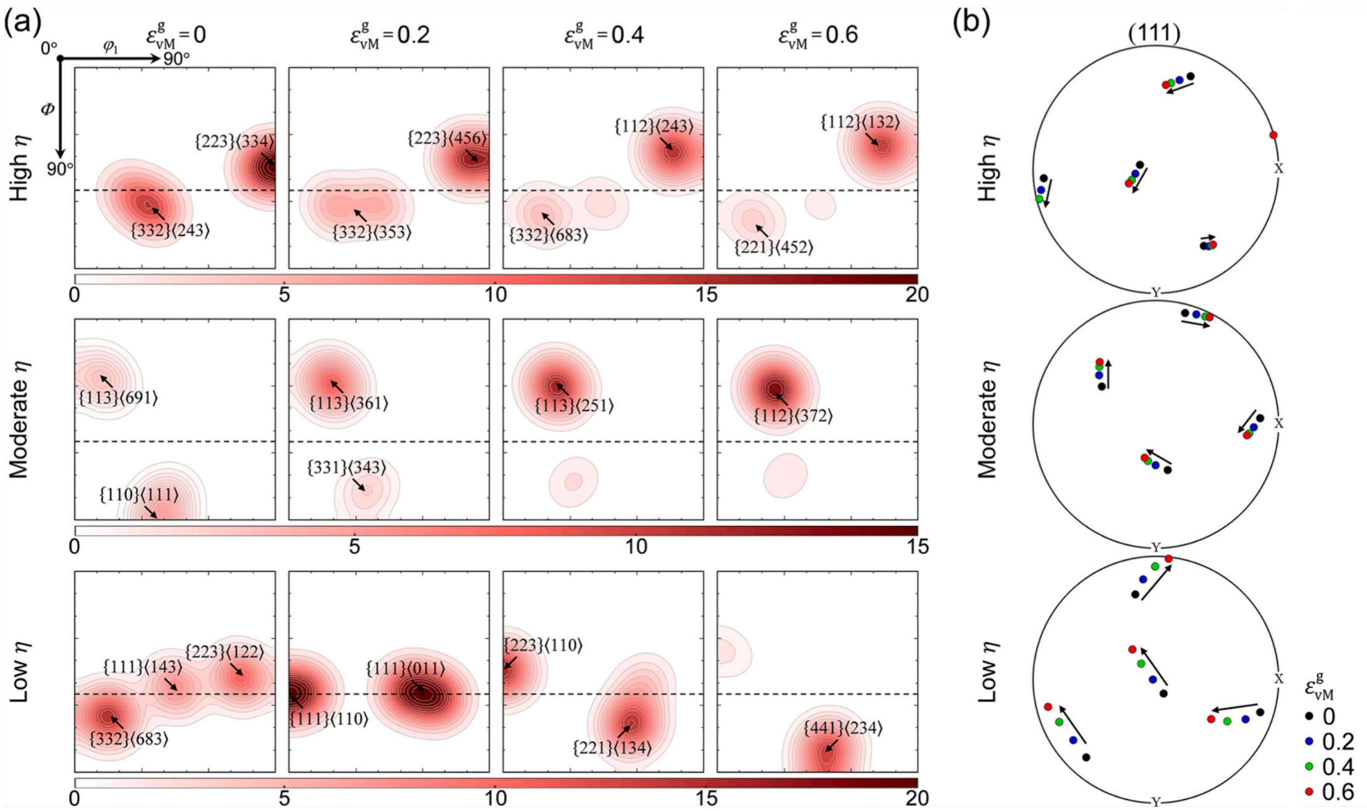

Fig. 13. (a) ODF sections at $\varphi_2 = 45^\circ$ showing orientation distributions of CGs in RVEs subjected to high, moderate and low η histories at ε_{vM}^{g} of 0, 0.2, 0.4 and 0.6; (b) (111) PFs showing lattice rotation trajectories of CGs in RVEs across stress states during deformation.

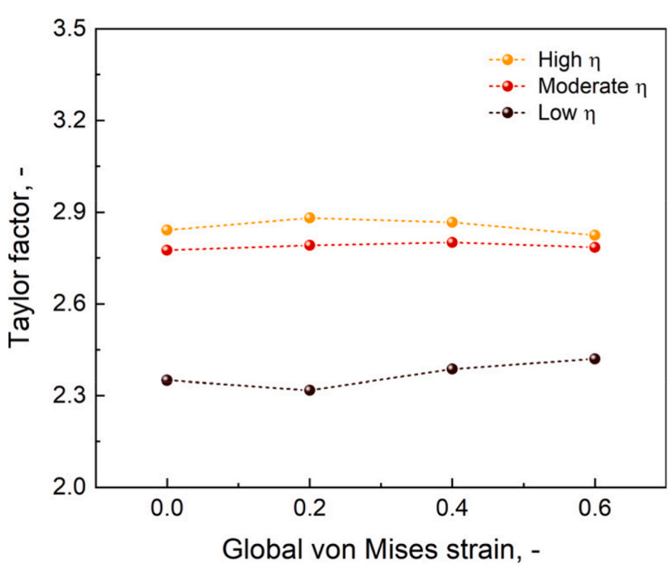

Fig. 14. Evolution of Taylor factor with deformation in CGs identified under high, moderate and low η loadings.

evolutions at three temperatures can be observed in Fig. 15. At the same ε_{vM}^{g} in Fig. 15 (a), CG3 yields the highest local strain by virtue of its soft nature under shear loading, i.e., low Taylor factor in Fig. 14. As deformation is inherently heterogeneous, local η evolutions could significantly deviate from global counterparts, as shown in Fig. 15 (b). It is worth noting that the fixed geometry discretization of the RVE throughout the simulation was not considered, which may induce extraneous computational errors due to the extreme distortion of some elements [59]. Therefore, the average response of each grain rather than a specific element is examined to improve our understanding of the material in the current study. Nevertheless, for more precise downscaling localization analysis, adaptive meshing techniques [18,60] that can overcome potential mesh distortion problem during large deformations need to be implemented for future research. Additionally, it should be noted that dislocation density evolution and strain gradient sensitivity are not included in the current CP simulations. To accurately capture the actual dislocation behavior due to the restriction of slip by martensite lath boundaries [61], a robust physics-based CP model incorporating these features is required, which is still under development.

5. Conclusions

Temperature-dependent deformation localization and failure in a low-carbon martensitic steel under various stress triaxiality loadings were systematically studied through a dual-scale modeling framework, combining macroscopic damage mechanics with CP simulations. The main conclusions are summarized as follows.

- A top-down macro-microscale modeling framework is proposed to address cross-scale deformation localization. Realistic boundary conditions are implemented to bridge the two scales, and the coupling between them is validated in terms of principal strain and stress triaxiality histories.
- The local ductility of the material at different temperatures is significantly affected by stress state. The material intrinsic fracture locus determined by the MBW model provides global fracture criteria for the RVE. The CPFE model reproduces the temperature-dependent flow behaviors by tuning the initial hardening rate, size-independent initial CRSS and saturation CRSS.

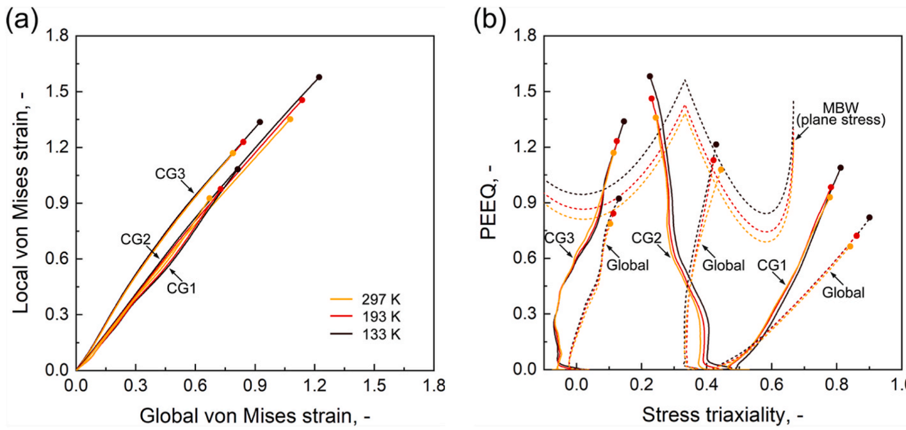

Fig. 15. Evolution of average local (a) strain and (b) η over CG1, CG2 and CG3 (solid lines). Evolution of global η in the corresponding RVEs and the MBW predicted fracture loci for plane stress conditions are also marked by dashed lines in (b) for reference. Yellow, red and black solid/dashed lines represent deformation cases at 297 K, 193 K and 133 K. Solid dots signify macroscopic failure moments.

- Lattice reorientation in the martensitic steel is less sensitive to temperature changes, irrespective of stress triaxiality. Texture evolution at RT is an accurate approximation for that under cryogenic conditions.
- Stress state distinctly influences lattice reorientation behavior. Deformation under shear loading, i.e., low η, facilitates lattice rotation with strengthened near rot-goss $\{110\}\langle 332\rangle$ and near brass $\{331\}\langle 136\rangle$ textures, whilst moderate and high η loadings drive relatively limited and uniform lattice rotation, giving rise to small orientation changes and homogeneous deformation.

CRediT authorship contribution statement

Zhen Zhang: Conceptualization, Methodology, Data curation, Formal analysis, Software, Validation, Visualization, Writing – original draft. **Sebastian Münstermann:** Supervision, Resources, Writing – review & editing. **Fuhui Shen:** Conceptualization, Methodology, Supervision, Validation, Visualization, Writing – review & editing.

Declaration of competing interest

The authors declare that they have no known competing financial interests or personal relationships that could have appeared to influence the work reported in this paper.

Acknowledgments

The financial support for the project (IGF.-Nr. 21094N/FOSTA P1359) by the German Federal Ministry for Economic Affairs and Energy based on a decision taken by the German Bundestag is greatly acknowledged. The authors would like to thank the "Forschungsvereinigung Stahlanwendung e.V. (FOSTA)" and the "Arbeitsgemeinschaft industrieller Forschungsvereinigungen e.V." for their support. Z. Zhang would like to acknowledge the financial support from China Scholarship Council (China, Grant No. 202006240048). Simulations were performed with computing resources granted by RWTH Aachen University (Germany) under project rwth0813.

Appendix

A. Temperature curves of experiments

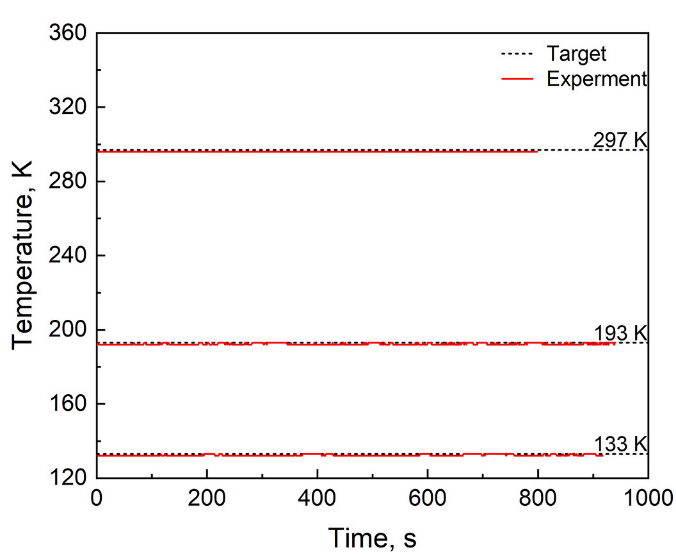

Fig. A1. Temperature curves of uniaxial tensile tests using smooth dog bone specimens performed at the targeted temperatures of 297 K, 193 K and 133 K.

B. Mesh sensitivity analysis

To clarify the effects of the element size on strain field distribution and stress triaxiality evolution, nine simulations were performed with varying element sizes of 1.4 μm, 1.2 μm and 1 μm under three different loadings for the investigated material. Fig. B1 shows the result of mesh sensitivity analysis. It is observed that decreasing the mesh size could slightly enhance the localization tendency while producing smoother strain fields. Results of stress triaxiality evolution reveal relatively small effects of the element size.

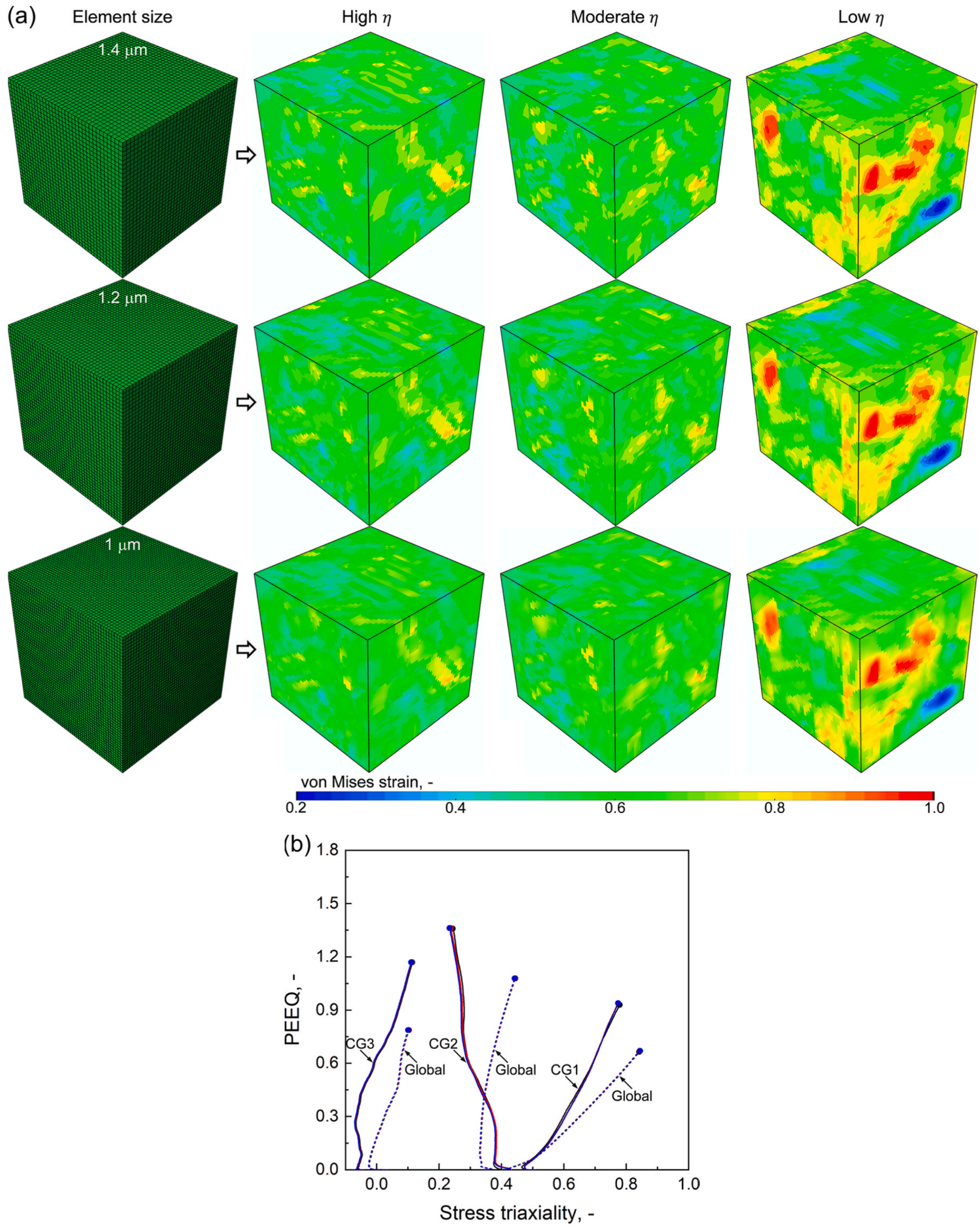

Fig. B1. (a) Effect of different mesh sizes on strain heterogeneities in deformed RVEs at ε_{vM}^{g} of 0.6 under high, moderate and low stress triaxiality loadings; (b) effect of different mesh sizes on the evolution of global and local stress triaxiality. Blue, red and black solid/dashed lines in (b) represent deformation cases using 1.4 μm, 1.2 μm and 1 μm. Solid dots indicate macroscopic failure moments.

Data availability

Data will be made available on request.

References

[1] Morito S, Tanaka H, Konishi R, Furuhara T, Maki T. The morphology and crystallography of lath martensite in Fe-C alloys. Acta Mater 2003;51(6):1789–99.
[2] Zhang Z, Shen FH, Liu HQ, Könemann M, Münstermann S. Temperature-dependent deformation and fracture properties of low-carbon martensitic steel in different stress states. J Mater Res Technol 2023;25:1931–43.
[3] Fischer T, Zhou T, Dahlberg CFO, Hedström P. Relating stress/strain heterogeneity to lath martensite strength by experiments and dislocation density-based crystal plasticity. Int J Plast 2024;174:103917.
[4] Krauss G. Martensite in steel: strength and structure. Mater Sci Eng A 1999;273:40–57.
[5] Feng H, Wang HJ, Li HB, Zhu HC, Zhang SC, Jiang ZH. Parent austenite grain reconstruction in martensitic steel. J Mater Sci Technol 2025;215:244–57.
[6] Spätig P, Bonadé R, Odette GR, Rensman JW, Campitelli EN, Mueller P. Plastic flow properties and fracture toughness characterization of unirradiated and irradiated tempered martensitic steels. J Nucl Mater 2007;367:527–38.
[7] Morris Jr JW. On the ductile-brittle transition in lath martensitic steel. ISIJ Int 2011;51(10):1569–75.
[8] Morsdorf L, Jeannin O, Barbier D, Mitsuhara M, Raabe D, Tasan CC. Multiple mechanisms of lath martensite plasticity. Acta Mater 2016;121:202–14.
[9] Tvergaard V. Influence of voids on shear band instabilities under plane strain conditions. Int J Fract 1981;17:389–407.
[10] Bai YL, Wierzbicki T. A new model of metal plasticity and fracture with pressure and Lode dependence. Int J Plast 2008;24(6):1071–96.
[11] Lian JH, Sharaf M, Archie F, Münstermann S. A hybrid approach for modelling of plasticity and failure behaviour of advanced high-strength steel sheets. Int J Damage Mech 2013;22(2):188–218.
[12] Shen FH, Münstermann S, Lian JH. A unified fracture criterion considering stress state dependent transition of failure mechanisms in bcc steels at –196°C. Int J Plast 2022;156:103365.
[13] Shen FH, Münstermann S, Lian JH. Cryogenic ductile and cleavage fracture of bcc metallic structures–influence of anisotropy and stress states. J Mech Phys Solids 2023;176:105299.
[14] Shen FH, Sparrer Y, Rao J, Könemann M, Münstermann S, Lian JH. A forming limit framework accounting for various failure mechanisms: localization, ductile and cleavage fracture. Int J Plast 2024;175:103921.
[15] Roters F, Eisenlohr P, Hantcherli L, Tjahjanto DD, Bieler TR, Raabe D. Overview of constitutive laws, kinematics, homogenization and multiscale methods in crystal plasticity finite-element modeling: theory, experiments, applications. Acta Mater 2010;58(4):1152–211.
[16] Park J, Hou Y, Min JY, Hou ZR, Han HN, He BB, Lee MG. Understanding plasticity in multiphase quenching & partitioning steels: insights from crystal plasticity with stress state-dependent martensitic transformation. Int J Plast 2024;180:104075.
[17] Chatterjee A, Sk MB, Ghosh A, Mitra R, Chakrabarti D. Combining crystal plasticity and electron microscopy to elucidate texture dependent micro-mechanisms of tensile deformation in lath martensitic steel. Int J Plast 2022;153:103251.
[18] Lypchanskyi O, Chiu CC, Qayyum F, Korpala G, Guk S, Chao CK, Prahl U. Temperature dependent deformation behavior and texture evolution in AA6082 aluminum alloy: an integrated experimental and crystal plasticity simulation approach. Int J Plast 2024;176:103942.
[19] Yang H, Li H, Ma J, Wei D, Chen J, Fu MW. Temperature dependent evolution of anisotropy and asymmetry of α-Ti in thermomechanical working: characterization and modeling. Int J Plast 2020;127:102650.
[20] Knezevic M, McCabe RJ, Lebensohn RA, Tomé CN, Liu C, Lovato ML, Mihaila B. Integration of self-consistent polycrystal plasticity with dislocation density based hardening laws within an implicit finite element framework: application to low-symmetry metals. J Mech Phys Solids 2013;61(10):2034–46.
[21] Zhang Z, Shen FH, Münstermann S. Crystal plasticity modeling of prior austenite orientation effects on deformation behaviors of martensitic steels under different strain paths. Mater Des 2024;245:113280.
[22] Ali U, Odoh D, Muhammad W, Brahme A, Mishra RK, Wells M, Inal K. Experimental investigation and through process crystal plasticity-static recrystallization modeling of temperature and strain rate effects during hot compression of AA6063. Mater Sci Eng A 2017;700:374–86.
[23] Liu Q, Roy A, Silberschmidt VV. Temperature-dependent crystal-plasticity model for magnesium: a bottom-up approach. Mech Mater 2017;113:44–56.
[24] Fang QH, Lu WZ, Chen Y, Feng H, Liaw PK, Li J. Hierarchical multiscale crystal plasticity framework for plasticity and strain hardening of multi-principal element alloys. J Mech Phys Solids 2022;169:105067.
[25] Hutchinson JW, Evans AG. Mechanics of materials: top-down approaches to fracture. Acta Mater 2000;48(1):125–35.
[26] Liu JN, Liu GS, Ye CQ, Chen KG, Hu JB, Yu YY, Shen Y. Multiscale investigation of shear relaxation in shock loading: a top-down perspective. Mater Des 2022;220:110839.
[27] Cheng JH, Hu XH, Lach T, Chen X. A macro-micro approach for identifying crystal plasticity parameters for necking and failure in nickel-based alloy haynes 282. Int J Plast 2024;178:103997.
[28] Wen JC, Wei YJ. Top-down constitutive modelling to capture nanoscale shear localization. J Mech Phys Solids 2024;187:105629.
[29] Horstemeyer MF, Baskes MI, Godfrey A, Hughes DA. A large deformation atomistic study examining crystal orientation effects on the stress-strain relationship. Int J Plast 2002;18(2):203–29.
[30] He JC, Zhu SP, Gao JW, Liu R, Li W, Liu Q, He Y, Wang QY. Microstructural size effect on the notch fatigue behavior of a Ni-based superalloy using crystal plasticity modelling approach. Int J Plast 2024;172:103857.
[31] Zhou Y, Fan QB, Liu X, Wang DD, Zhu XJ, Chen K. Multi-scale crystal plasticity finite element simulations of the microstructural evolution and formation mechanism of adiabatic shear bands in dual-phase Ti20C alloy under complex dynamic loading. J Mater Sci Technol 2020;59:138–48.
[32] Meade ED, Sun FW, Tiernan P, O'Dowd NP. A multiscale experimentally-based finite element model to predict microstructure and damage evolution in martensitic steels. Int J Plast 2021;139:102966.
[33] Niessen F, Nyyssönen T, Gazder AA, Hielscher R. Parent grain reconstruction from partially or fully transformed microstructures in MTEX. J Appl Crystallogr 2022;55(1):180–94.
[34] Hielscher R, Nyyssönen T, Niessen F, Gazder AA. The variant graph approach to improved parent grain reconstruction. Materialia 2022;22:101399.
[35] Kurdjumov G, Sachs G. über den Mechanismus der Stahlhärtung. Zeitschr Phys 1930;64:325–43.
[36] DIN EN ISO 6892-1: Metallische Werkstoffe–Zugversuch. Teil 1: prüfverfahren bei Raumtemperatur. Berlin: DIN e.V; 2016.
[37] DIN EN ISO 6892-3: Metallische Werkstoffe–Zugversuch. Teil 3: prüfverfahren bei tiefen Temperaturen. Berlin: DIN e.V; 2015.
[38] Habibi N, Vajragupta N, Münstermann S. Deformation and damage assessments of two DP1000 steels using a micromechanical modelling method. Crystals 2021;11(7):805.
[39] Henrich M, Pütz F, Münstermann S. A novel approach to discrete representative volume element automation and generation-DRAGen. Materials 2020;13(8):1887.
[40] Barsanescu P, Sandovici A, Serban A. Mohr-Coulomb criterion with circular failure envelope, extended to materials with strength-differential effect. Mater Des 2018;148:49–70.
[41] Wu B, Li X, Di Y, Brinnel V, Lian JH, Münstermann S. Extension of the modified Bai-Wierzbicki model for predicting ductile fracture under complex loading conditions. Fatigue Fract Eng Mater Struct 2017;40(12):2152–68.
[42] Lu YS, Zhu ZW, Li DY, Xie QJ. Constitutive model of 42CrMo steel under a wide range of strain rates based on crystal plasticity theory. Mater Sci Eng A 2017;679:215–22.
[43] Sedighiani K, Traka K, Roters F, Raabe D, Sietsma J, Diehl M. Determination and analysis of the constitutive parameters of temperature-dependent dislocation-density-based crystal plasticity models. Mech Mater 2022;164:104117.
[44] Fromm BS, Adams BL, Ahmadi S, Knezevic M. Grain size and orientation distributions: application to yielding of α-titanium. Acta Mater 2009;57(8):2339–48.
[45] Pei YB, Hao YG, Zhao J, Yang JT, Teng BG. Texture evolution prediction of 2219 aluminum alloy sheet under hydro-bulging using cross-scale numerical modeling. J Mater Sci Technol 2023;149:190–204.
[46] Wang MY, Wu JJ, Qian ZH, Wu W, Yang ZK, Liu L, Wang H. Texture and bendability evolution mechanism of 6063 aluminum alloy tube formed by free-bending technology employing cross-scale numerical modeling. J Mater Process Technol 2024;332:118568.
[47] Shen FH, Wang HS, Liu ZJ, Liu WQ, Könemann M, Yuan G, Wang GD, Münstermann S, Lian JH. Local formability of medium-Mn steel. J Mater Process Technol 2022;299:117368.
[48] Azzeddine H, Bradai D, Baudin T, Langdon TG. Texture evolution in high-pressure torsion processing. Prog Mater Sci 2022;125:100886.
[49] Ghorbanpour S, Alam ME, Ferreri NC, Kumar A, McWilliams BA, Vogel SC, Bicknell J, Beyerlein IJ, Knezevic M. Experimental characterization and crystal plasticity modeling of anisotropy, tension-compression asymmetry, and texture evolution of additively manufactured Inconel 718 at room and elevated temperatures. Int J Plast 2020;125:63–79.
[50] Cyr ED, Mohammadi M, Mishra RK, Inal K. A three dimensional (3D) thermo-elasto-viscoplastic constitutive model for FCC polycrystals. Int J Plast 2015;70:166–90.
[51] Knezevic M, McCabe RJ, Tomé CN, Lebensohn RA, Chen SR, Cady CM, Gray Iii GT, Mihaila B. Modeling mechanical response and texture evolution of α-uranium as a function of strain rate and temperature using polycrystal plasticity. Int J Plast 2013;43:70–84.
[52] Ibragimova O, Brahme A, Muhammad W, Lévesque J. A new ANN based crystal plasticity model for FCC materials and its application to non-monotonic strain paths. Int J Plast 2021;144:103059.
[53] Rakshit R, Sarkar A, Panda SK, Mandal S. Influence of out-of-plane stretch forming induced different strain paths on micro-texture evolution, slip system activity and Taylor factor distribution in Al–Li alloy. Mater Sci Eng A 2022;830:142267.
[54] Jiang J, Britton TB, Wilkinson AJ. The orientation and strain dependence of dislocation structure evolution in monotonically deformed polycrystalline copper. Int J Plast 2015;69:102–17.
[55] Yerra SK, Vankudre HV, Date PP, Samajdar I. Effect of strain path and the magnitude of prestrain on the formability of a low carbon steel: on the textural and microtextural developments. J Eng Mater Technol 2004;126(1):53–61.
[56] Hayakawa Y, Szpunar JA. A comprehensive model of recrystallization for interstitial free steel. Acta Mater 1997;45(9):3721–30.
[57] Na H, Nambu S, Ojima M, Inoue J, Koseki T. Strain localization behavior in low-carbon martensitic steel during tensile deformation. Scripta Mater 2013;69:793–6.

[58] Raabe D, Sachtleber M, Zhao Z, Roters F, Zaefferer S. Micromechanical and macromechanical effects in grain scale polycrystal plasticity experimentation and simulation. Acta Mater 2001;49(17):3433–41.

[59] Kim DK, Kim JM, Park WW, Lee HW, Im YT, Lee YS. Three-dimensional crystal plasticity finite element analysis of microstructure and texture evolution during channel die compression of IF steel. Comput Mater Sci 2015;100:52–60.

[60] Sedighiani K, Traka K, Roters F, Sietsma J, Raabe D, Diehl M. Crystal plasticity simulation of in-grain microstructural evolution during large deformation of IF-steel. Acta Mater 2022;237:118167.

[61] Michiuchi M, Nambu S, Ishimoto Y, Inoue J, Koseki T. Relationship between local deformation behavior and crystallographic features of as-quenched lath martensite during uniaxial tensile deformation. Acta Mater 2009;57(18):5283–91.